Int. J. of Thermal & Environmental Engineering
Volume 20, No. 1 (2023) 13-19

Single plate analysis of thermoacoustic refrigerator

Omar Al-Mufti[a] and Isam Janajreh[a*]

[a] *Department of Mechanical Engineering, Khalifa University of Science and Technology, Abu Dhabi, UAE*

Abstract

Thermoacoustic refrigerator (TAR) or heat pump is a device that uses acoustic sound to pump heat from a lower temperature reservoir. The most distinct feature of thermoacoustic systems is that they do not have moving parts, which makes them reliable with no to low maintenance. TAR can be driven using thermoacoustic engine (TAE) in which the later can be sustainably operated utilizing waste heat or concentrated solar. Also, in contrary to conventional refrigeration methods, TARs do not use environmentally harmful gasses. In this work, a high-fidelity localized model is developed to simulate the flow in a standing wave (straight tabular) thermoacoustic refrigerator. In this localized analysis a subsection domain that runs through two stack halves and stretches nearly 1.5 stack length at each side is considered. The acoustic waves were simulated using oscillating walls at the two domain limits at a given resonance frequency. The model compared favorably to previous experimental and numerical findings. The analysis was done for drive ratios in range of 0.28% to 2%. A 3.2 ºC temperature difference is produced at the 2% drive ratio compared to 0.5 ºC at the 0.28% ratio. Higher difference can be achieved at higher drive ratio and also larger stack length.

Keywords: *Numerical modeling; Thermoacoustic; Refrigerator; Drive ratio; CFD*

Nomenclature

a	Fluid's speed of sound
B	Blockage ratio (porosity)
c_p	Specific heat
COP	Coefficient of Performance
D	Drive ratio
f	Frequency
h	Plate spacing
L	Plate/Stack length
k	Wave number
K	Thermal conductivity
T	Temperature
p	Pressure
R	Gas constant
t	Time / Plate thickness
u	Axial velocity (in x-direction)
V	Velocity vector
Δy	Vertical element size

Greek Symbols

μ	Dynamic viscosity
γ	ratio of isobaric to isochoric specific heats (c_p/c_v)
ρ	density
ω	Angular frequency
δ_k	Thermal penetration depth
λ	Wave length
ϕ	Phase angle

Subscripts and Superscripts

0	Amplitude
g	Fluid
m	Mean value
p	Solid (plate)

1. Introduction

Thermoacoustic refrigerator (TAR) or heat pump is a device that utilizes acoustic energy to pump heat from a lower temperature reservoir. Fig. 1 show a schematic for a TAR. It consists of a resonant tube filled with a working gas such as air, He, Arg. CO2 or their mixtures, cold and hot heat exchangers, a stack, and an acoustic driver. The acoustic driver generates sound waves that travel through the gas, causing it to expand and contract. Thus, acoustic waves can be described as coupled pressure and displacement oscillations [1]. The temperature also oscillates due to the variation in pressure. TAR is a potential sustainable method for cooling due to the following: TAR's are reliable due to the absence of moving parts [1], their manufacturing is easy and inexpensive, and they utilize environmental-friendly gasses, such as Helium and Air. Additionally, TARs could operate on waste or solar heat [2]. This is done through a Thermoacoustic

* Corresponding author. Tel.: +971023123286
Fax: +9876543210; E-mail: Isam.Janajreh@ku.ac.ae

DOI: 10.5383/ijtee.20.01.003

engine (TAE) that converts solar/waste heat into the acoustic power required by the TAR. Moreover, TAR's are very promising in various applications, such as Air conditioning for buildings and vehicles [3,4], natural gas liquefication [5,6], and electronics cooling [7-10] which is done through miniaturized compact designs. Thermoacoustic devices can be classified based on the type of wave, i.e., standing wave and traveling wave systems. What differentiates a traveling wave from standing wave is the phasing between pressure and velocity oscillations, where the phasing is 0° for travelling wave systems, and 90° for standing wave systems. Moreover, in traveling wave systems, the stack is called regenerator. The difference between the regenerator and the stack is that the stack has poor thermal contact with the working fluid, while the regenerator has perfect thermal contact. Thus, traveling wave can attain higher efficiencies. Standing wave systems, which are the focus of this study, usually have a straight tabular design. The thermodynamic cycle of a standing wave TAR is shown in Fig. 2, and it has the following the steps:

- A-B: Isentropic compression
- B-C: heat rejection
- C-D: Isentropic expansion
- D-A: heat addition

A detailed theory of thermoacoustic was firstly introduced by Nikolaus Rott in 1969 [11], who then summarized his results in 1980 review [12]. Additionally, a comprehensive review and analysis of thermoacoustic technology was done by Swift [1,13]. These publications can be considered as the basis of thermoacoustic. Moreover, recent review papers spotlight the current advancements in thermoacoustic technology [14,15]. The aforementioned studies are recommended for those who seek more fundamental and theoretical understanding of thermoacoustic. The current study focuses mainly on simulating the TAR numerically using Computational Fluid Dynamics (CFD).

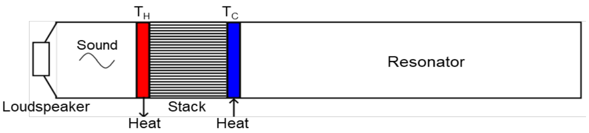

Fig. 1. a) Thermoacoustic engine b) Thermoacoustic refrigerator

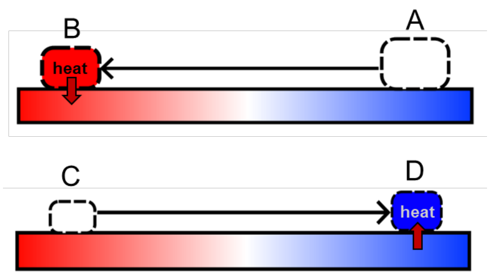

Fig. 2. Standing wave Thermoacoustic refrigerator cycle

Several numerical studies have been done on TARs. Rahpeima and Ebrahimi [16] studied the effect of changing different geometrical and thermophysical parameters on the TAR performance. The computational domain consisted of only one plate with symmetrical top and bottom boundaries, and the drive ratio was limited to 1.7%. The study concluded that optimum spacing between the plates was 3.33 δ_k . δ_k is the thermal penetration depth. It was also found that increasing the heat capacity of stack increases the time the TAR needs to reach steady state, while decreasing the thermal conductivity resulted in increasing the temperature difference but decreasing the COP. Marx and Blanc-Benon [17] simulated a TAR and investigated the effect of some geometrical parameters and acoustic Mach number on the performance. The computational domain included a zero-thickness isothermal plate and heat exchangers. At relatively high Mach numbers, there was a non-linear distortion of the temperature oscillations above the plate. Additionally, it was found that both the cold heat exchanger length and the gap between it and the plate should be close to the displacement amplitude. Zoontjens et al. [18] studied thermoacoustic couple performance with modified plate edges. It was found that stack plates with streamlined edges improve the rate of heat transfer only at low drive ratios. Stack plates with aerofoil shaped edges achieved the highest temperature difference at all drive ratios. Compared to other edge shapes, rounded edge was recommended as the most practical, due to its easier manufacturing and the outperforming COP at all drive ratios. Cao et al. [19] was one of the first who numerically simulated the energy flux in thermoacoustic couples. The soundwave was simulated by imposing oscillating velocity at the inlet and outlet of the domain. The inlet/outlet boundaries were also adiabatic. Thus, as per Cao et al. [19], these boundary conditions can be described as sinusoidally moving, thermally insulated pistons. Cao also noted that these boundary conditions may not mimic the exact local physical process, however, they emulate the far field of the plate in a thermoacoustic couple reasonably, ensuring that the distance from the boundaries to the plate is long enough. As for simulating the sound wave in the computational domain, oscillating boundary conditions are usually used, where either oscillating velocity or pressure is imposed and the other is calculated. It was found by Besnoin [20] that at high drive ratios, velocity boundary conditions result in a sustained drift in mean pressure, temperature, and density values. Thus, it was suggested that oscillating pressure is more suitable for high drive ratios. Tisovsky and Vit [21] modelled the loudspeaker by modelling the motion of the membrane using OPENFOAM. As for thermoacoustic couples, it was suggested by Ishikawa and Mee [22] that oscillating boundary walls would by suitable to simulate the soundwave in the system. Abd El-Rahman and Abd El-Rahman [23] used a dynamic mesh to mimic the soundwave near thermoacoustic couples. Furthermore, it was noticed that most studies are limited to parallel plate stacks, and relatively low pressure amplitudes.

2. Model Development

2.1. Computational domain

A localized computational model of a thermoacoustic refrigerator (TAR) is used as a subset of the complete system. As shown in Fig. 3, the full system has a stack made of parallel plates and is asymmetrical. The localized domain is periodic and includes only half plate at top and bottom of the domain. This was done to reduce the size of the heat conjugated computational domain which will be pursued unsteadily. It also allows the usage of periodic boundary conditions. The distance to the right and left of the stack were chosen to be approximately 0.0085λ a following the work of Cao et al. [19]. Where $\lambda = a/f$ is the wavelength and $a = \sqrt{\gamma RT}$ is the speed of sound in the working fluid. The plate length (L) is 6.85 mm located at the center of the domain that stretches 31.784 mm. The plate thickness (t) is 0.1905 mm with spacing (h) of 1.3395mm and that corresponds to a blockage ratio ($B = \frac{h}{h+t}$) of 87.55%. The aforementioned geometrical stack parameters are similar to the TAR experimentally studied by [24]

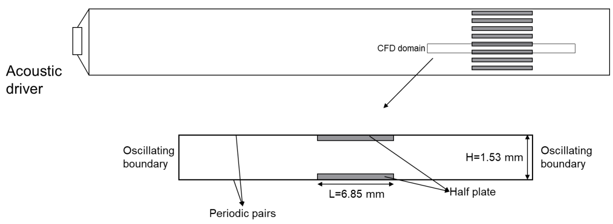

Fig. 3: Schematic of a TAR system and the computational domain

2.2. Governing equations

The numerical model solves a transient, non-isothermal, conjugated heat in turbulent regime flow. The simulations are governed by continuity (Eq.1), momentum (Eq. 2) (Navier-stokes), and internal energy (Eq. 3) equations:

$$\frac{\delta\rho}{\delta t} + \nabla.(\rho\vec{V}) = 0 \quad (1)$$

$$\left[\frac{\partial(\rho\vec{V})}{\partial t} + \nabla.(\rho\vec{V}\vec{V})\right] = -\nabla p + \nabla.\mu[(\nabla\vec{V} + \nabla\vec{V}^T) - \frac{2}{3}\nabla.\vec{V}I] + \rho\vec{g} \quad (2)$$

$$\frac{\partial(\rho E)}{\partial t} + \nabla.\left(\rho\vec{V}(\rho E + p)\right) = -\nabla.\left[K\nabla T + \left(\mu(\nabla\vec{V} + \nabla\vec{V}^T) - \frac{2}{3}\nabla.\vec{V}I\right)\vec{V}\right] \quad (3)$$

Where ρ is density, p is pressure,μ is dynamic viscosity, T is temperature, K is thermal conductivity, and t is time. Turbulence is accounted for following the averaging of these equations where the resulted Reynolds stresses $(-\rho V_i' V_j')$ are modelled via the common eddy viscosity k-ε per Eq. 4.

$$-\rho V_i' V_j' = \mu_t\left(\frac{\partial V_i}{\partial V_j} + \frac{\partial V_j}{\partial V_i}\right) \quad (4)$$

Where $\vec{V}$ is the velocity vector, I is the unit tensor and the term is the effect of volume dilation and $\rho\vec{g}$ is the body forces, E is the internal energy, μ_t is turbulent viscosity. The general transport equation following the common eddy viscosity model is expressed as:

$$\frac{\partial(\rho\emptyset)}{\partial t} + \nabla.(\rho\vec{V}\emptyset - \Gamma\nabla\emptyset) = S_{\emptyset_k} \quad (5)$$

In which $\emptyset$ can represent either the turbulence kinetic energy (k) or the dissipation rate (ϵ) whereas Γ is the diffusion coefficient and S is a source term related to k or ϵ.

2.3. Boundary conditions

Since the computational domain represents only one plate, and the full stack is just a repetition of this domain, as shown in Fig. 4, top and bottom surfaces were assigned as conformal periodic pairs. As for the plate walls that are in contact with the fluid, no-slip and conjugated heat transfer boundary conditions were applied, which are described as per the following equations:

$$T_{g,wall} = T_{p,wall} \quad (6)$$

$$K_g\frac{\partial T_g}{\partial n} = K_p\frac{\partial T_p}{\partial n} \quad (7)$$

$$u = 0 \quad (8)$$

Where u is the axial velocity (in x-direction), n is the local coordinate normal to the wall, and g and p subscripts corresponds to gas and plate, respectively. To simulate a standing wave following the work of Cao et al. [19] and Worlikar et al. [25], the oscillating boundaries were set as moving oscillating adiabatic walls $\left(\frac{\partial T}{\partial x} = 0\right)$ that represent the ideal motion of a gas parcel in a standing wave system. They oscillate per the following equations:

$$\text{Left wall: } u = \frac{p_0}{\rho_m a}sin(kx_{AB})\cos(\omega t) \quad (9)$$

$$\text{Right wall: } u = \frac{p_0}{\rho_m a}sin(kx_{CD})\cos(\omega t) \quad (10)$$

Where x_{AB} are x_{CD} the distance from the pressure antinode to the oscillating boundary, ω is the angular frequency ($\omega = 2\pi f$), k here is the wave number ($k = \frac{\omega}{a}$), and the subscripts m and 0 indicate mean and amplitude values, respectively. The stack midpoint was placed at a position of $kx = \frac{3\pi}{4}$ from the pressure antinode. The movement of the walls was done by using a layering dynamic mesh.

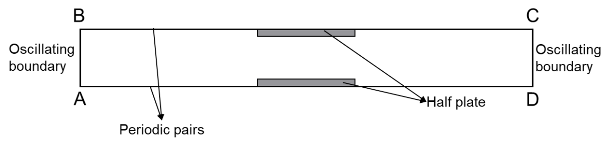

Fig. 4: Computational domain and boundary conditions

The simulations were developed using Ansys/Fluent, where a coupled pressure-velocity solver is used. All variables were discretized using 2nd order upwind, except for the pressure which was discretized using Pressure Staggering Option (PRESTO). The time step size was chosen to be between $\frac{\tau}{100}$ and $\frac{\tau}{200}$, as it was indicated by previous studies [18,23]. This small timestep size is required to capture the thermoacoustic phenomena accurately with τ is the reciprocal of the operating frequency (*f*) of the system (696 Hz) that corresponds to a timestep size of 1e-5. This is also equivalent to 144 data points for each acoustic cycle. The simulations were done for a non-isothermal plate, where a conjugated heat transfer between solid and fluid was applied.

For validation purposes, the numerical model was developed to simulate the thermoacoustic couple that have been studied experimentally by Atchley et al. [24] and numerically by Worlikar et al. [25]. The performance metric in such systems is the temperature difference developed along the plate.

2.4. Operating conditions

The system's working fluid is helium, while the plate is made of stainless steel epoxied with fiberglass. The helium is at 298.4 K and 114.1 kPa and assumed follows compressible ideal gas behavior. The system resonates at a frequency of 696 Hz. Additionally, four drive ratios ($D=p_o/p_m$) are considered, i.e. 0.28%, 0.5%, 1%, and 2%. Regarding the plate, its effective properties are listed in Table 1 [25]:

Table 1: Thermophysical properties of the plate

Density	Thermal conductivity	Heat capacity
5082 kg/m^3	5.76 W/m.K	683.5 J/Kg.K

To evaluate the mesh quality, the domain initially discretized in a medium resolution unstructured and hybrid (quadrilateral and triangular) finite volumes comprised of 11,469 elements. A finer mesh for the domain of quadrilateral type comprising 18,600 elements is also created. These are depicted in Fig. 5 where in both meshes the perpendicular yellow line denotes the extend of the thermal penetration depth from the plate. It highlights the most pronounced thermoacoustic region which seems is well represented/captured by the fine mesh. The thermal penetration depth (δ_k) is calculated as per the following equation:

$$\delta_k = \sqrt{2K_g/\omega\rho_m c_p} \tag{11}$$

Where c_p is the heat capacity of the working fluid. The average vertical size (Δy) of elements are within the size of the thermal penetration depth, that is 0.034 mm for the medium size mesh and 0.023 mm for the finer mesh, which corresponds to $\Delta y = \frac{\delta_k}{8.02}$ and $\Delta y = \frac{\delta_k}{11.85}$, respectively. Compared to previous studies, Cao et al. [19] used a $\Delta y = \frac{\delta_k}{11.54}$ and Marx and Blanc-Benon [26] used a $\Delta y = \frac{\delta_k}{10}$. Fig. 6 shows the temperature difference developed for both meshes. As both meshes are within the stipulated thermal penetration length they give reasonable temperature difference, but with slightly better results in favor of the finer mesh. Thus, the finer mesh will be used for the rest of the analysis. It can be also seen from Fig. 6 that it took 4 seconds of physical time for the temperatures at the hot and cold sides to converge. Accordingly, the proceeding analysis will continue until reaching a flow time of minimum 4 seconds.

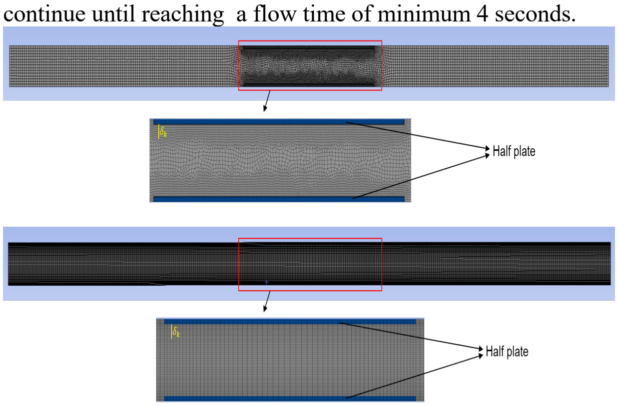

Fig. 5: Medium hybrid (top) and fine structured (bottom) meshes, full and plate close up views

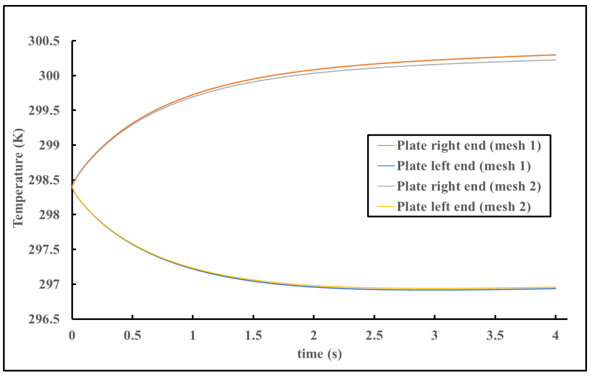

Fig. 6: Temperature gradient evolution at plate ends for both meshes

3. Results and discussion

As for the comparison with the previous studies [24,25], Fig. 7 shows the previous experimental and numerical results alongside the current developed model results. It can be clearly noticed that at drive ratio of 1% and lower, the model has high accuracy. However, at drive ratio of 2%, the difference between the current study and previous ones becomes clearer. In general, the deviation of the numerical results from the experimental is due firstly to the fact that the numerical model excludes the possible losses occur in experiments and that would lead to higher temperature difference. Secondly, looking at the operating conditions for the system mentioned in [25], it can be noticed that the helium properties are a bit different than the theoretical values, especially for the speed of sound, which was 1160 m/s instead of 1016.9 m/s. Suggesting a mixture rather pure helium gas which affects the fluid properties significantly. This will also influence the boundary conditions. Moreover, the theoretical temperature difference for pure helium would be slightly higher compared to the theoretical values shown in Fig. 7 that were calculated by Worlikar et al. [25]. The difference becomes higher at larger drive ratios, which might be the reason for a larger error at 2% drive ratio. Furthermore, applying a moving wall boundary condition results in a sustained drift in mean pressure of the system. This drift is noticeable at 2% drive ratio, but almost negligible at drive ratio inferior to 1%. A similar drift was noticed by Besnoin [20] when applying an oscillating velocity boundary condition attributing to the discrepancies at larger drive ratios. Nevertheless, the error is within acceptable range rendering the confidence to utilize the computational domain for further studies.

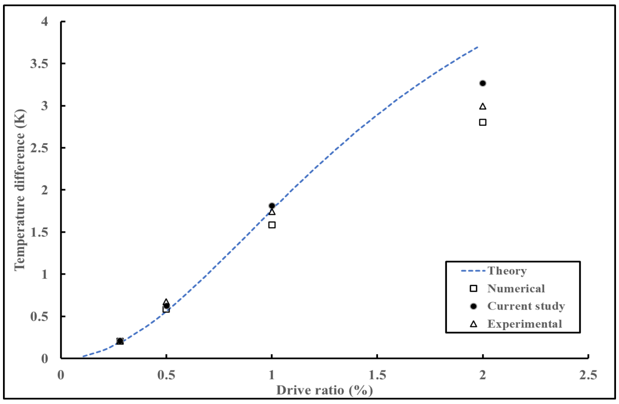

Fig. 7: Comparison of the obtained temperature gradient with previous numerical/experimental work [24,25]

Fig. 8 depicts the temperature gradient along the plate at different drive ratios. As expected, the temperature gradient increases with increasing the drive ratio. It can be also noticed that the gradient is slightly deviating from the linear trend as the drive ratio increases significantly. Markedly, at lower drive ratios (0.28% & 0.5%), the change in temperature at both ends is equivalent, and the temperature at the middle of plate is at the same value as the mean temperature. However, at drive ratio of 2% for instance, the temperature rise at the hot side is higher than the temperature descend at the cold side. Thus, the temperature at the middle of the plate is higher than the mean temperature. Fig. 9 shows the heat flux along the plate. It can be seen that the heat flux is almost zero anywhere along the plate, except at the ends, where it reaches the maximum. Similar to the temperature difference, the heat flux increases with increasing the drive ratio.

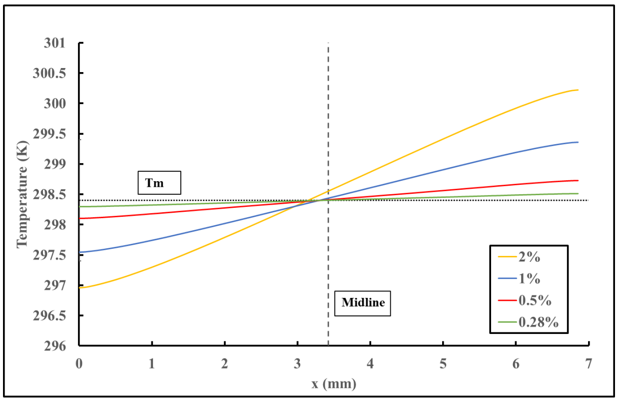

Fig. 8: Temperature gradient along the plate for different drive ratios

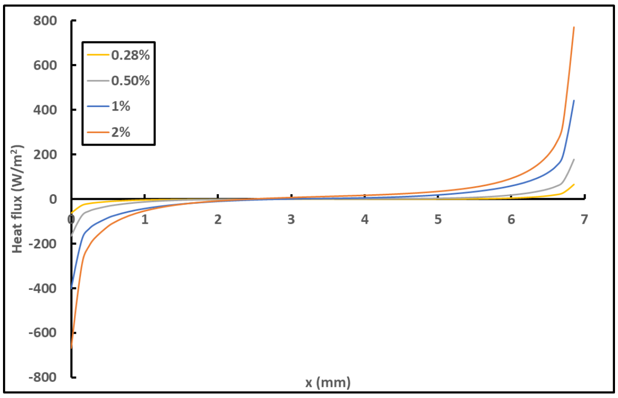

Fig. 9: Heat flux along the plate for different drive ratios

Furthermore, Fig. 10 shows the mean (time averaged over one acoustic cycle) axial velocity at the middle of the domain wrt position in y-direction. Where a y value of zero is at the bottom of the first half-plate, while a value of 1.53 mm is at the top of the second half-plate. This explains the zero values at top and bottom of the figure. Between the plates, the values are supposed to be nil as well. However, it can be noticed that there are non-zero values for all drive ratios. The non-zero values are more significant at the highest drive ratio (2%). A similar behavior was observed by Abd El-Rahman and coworker [23] under the same operating conditions.

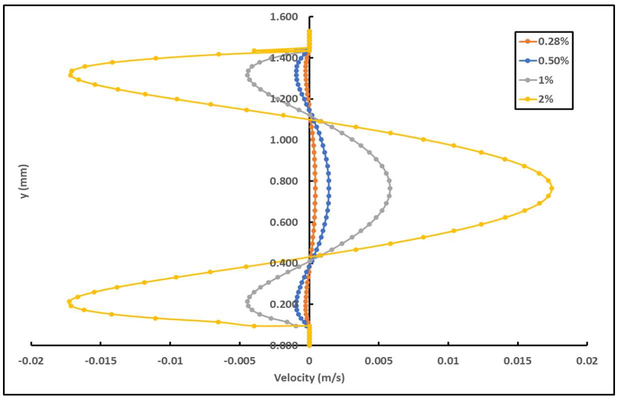

Fig. 10: Mean axial velocity at plate's midline for different drive ratios

Fig. 12 illustrates the velocity vector field near the hot end of the stack at different phases (Φ). Where the behavior of the axial velocity during one acoustic period is shown in Fig. 11. It can be noticed from Fig. 12 that small circulations are appearing near stack edges between 134° and 158°. These two counter-rotating vortices, generated behind the plate, are the result of flow separation. The circulations move to the middle and become larger at 180° when the flow is about to switch direction. Time averaging these vector fields over one acoustic cycle results in what is shown in Figs 13.a to 13.d. Figures 13.a. 13.b, 14.c, 13.d show the mean vorticity contour alongside the mean velocity vector filed for drive ratios of 0.28%, 0.5%, 1%, and 2%, respectively. It can be noticed that vorticity increases with increasing the drive ratio. The vortices become less circular and have a larger area at higher drive ratios. The velocity values are also higher at higher drive ratios.

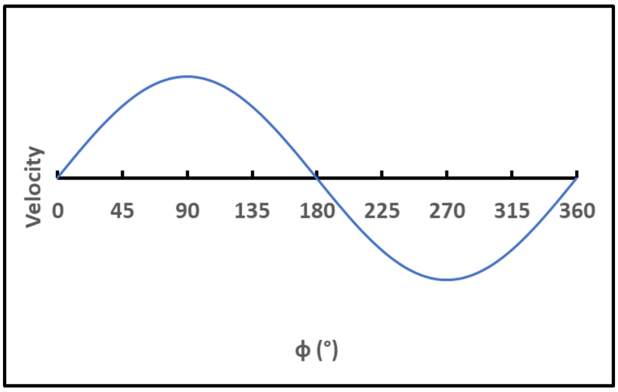

Fig. 11: Axial velocity behavior over single acoustic cycle

5. Conclusion

Localized numerical simulations were done for a thermoacoustic refrigerator (TAR). The results achieved reasonable accuracy compared to the previous studies. This gives enough confidence to utilize this model for future work and further sensitivity studies. The results showed that using the moving walls at higher drive ratios results in sustained drift in the mean pressure of the domain. Furthermore, results reveal that the temperature gradient increased with increasing the drive ratio. The highest temperature difference was around 3 ℃ at 2% drive ratio. The low temperature difference is mainly due to the short stack (6.85 mm). The velocity vector field showed that from phases 0◦ to 180◦, at the plate's hot end, the fluid rolls up around the sharp edges of the plates, due to flow separation. Thus, two counter-rotating vortices are generated behind the plate. Moreover, increasing the drive ratio increased the vorticity near the plate edges. Global but coarse analysis can be pursued economically in the future to have a better view for the flow field near the stack, especially at high drive ratios and determining the boundary conditions and carry out further local analysis more accurately.

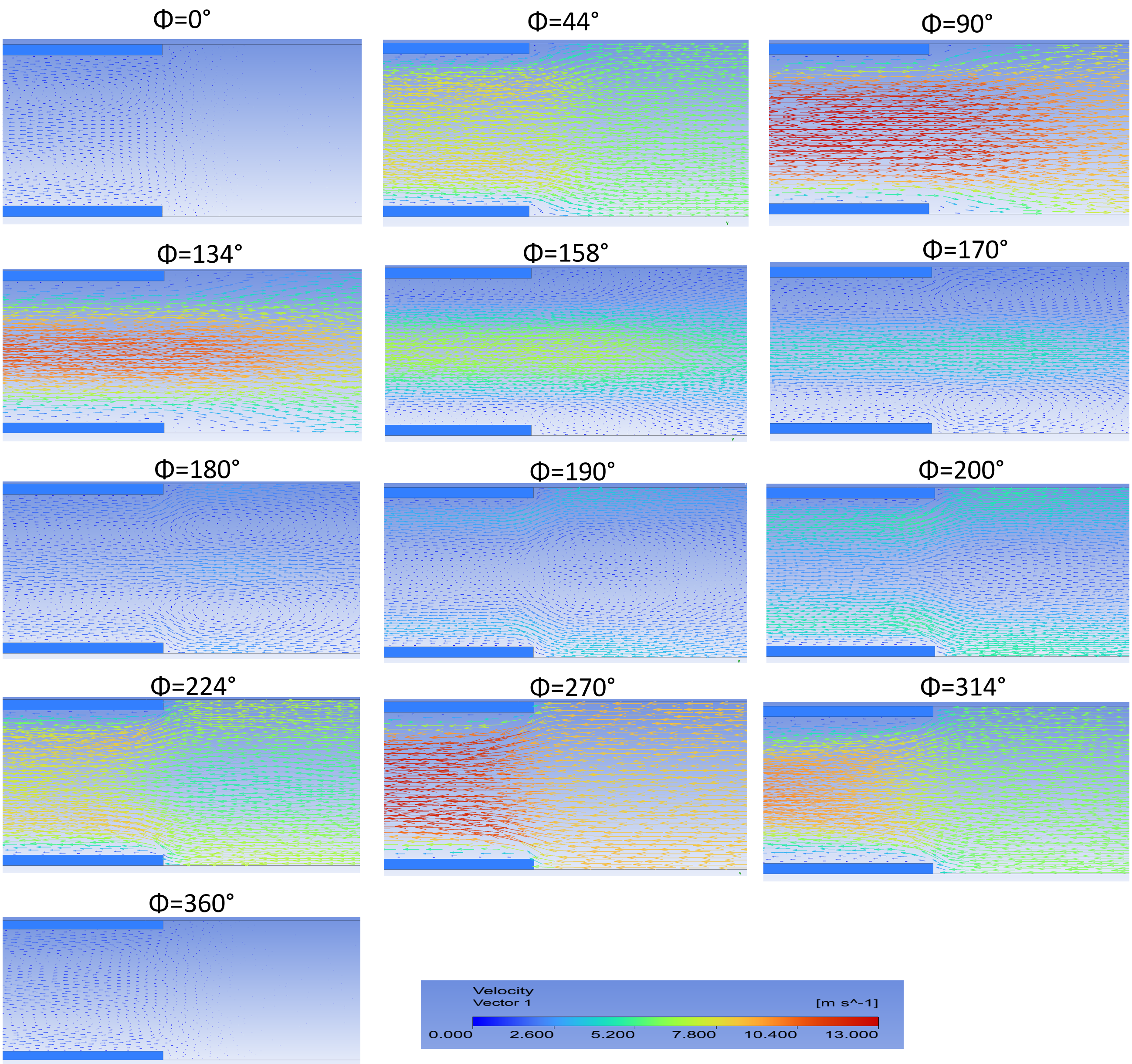

Fig. 12: Velocity vector field at different phases over one acoustic cycle

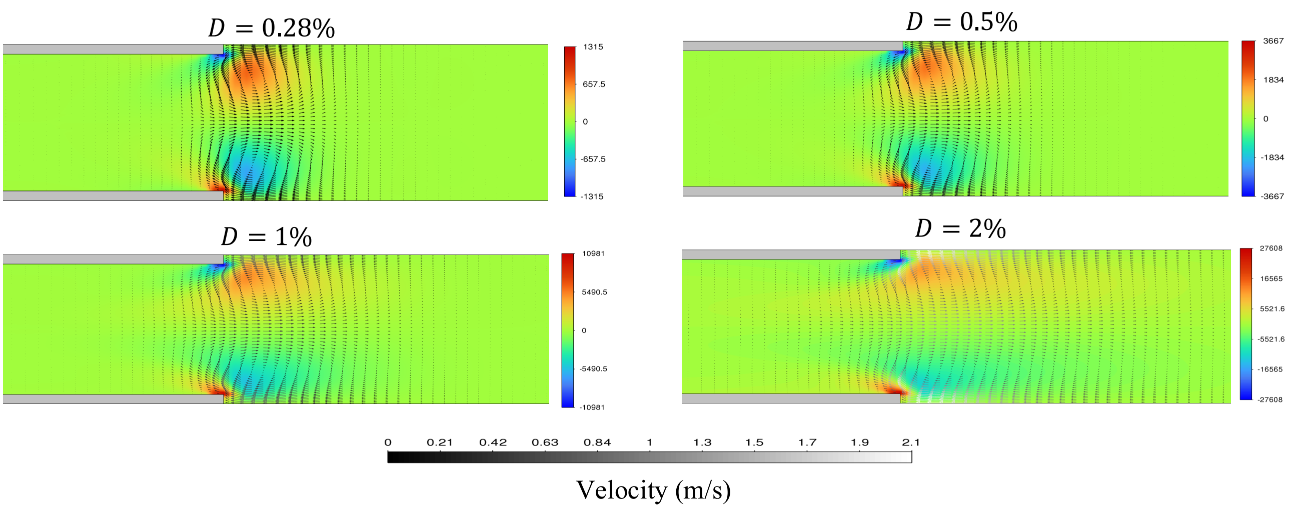

Fig. 13: Mean vorticity contour and mean velocity vector field for a) D=0.28% b) D=0.5% c) D=1% d) D=2%

References

[1] G. W. Swift, *Thermoacoustics*. Cham: Springer International Publishing, 2017. Accessed: Jul. 08, 2022. [Online]. Available: http://link.springer.com/10.1007/978-3-319-66933-5

[2] J. A. Adeff and T. J. Hofler, "Design and construction of a solar- powered, thermoacoustically driven, thermoacoustic refrigerator," *Acoustics Research Letters Online*, p. 6, 2000.

[3] H. Wang *et al.*, "A looped heat-driven thermoacoustic refrigeration system with direct-coupling configuration for room temperature cooling," *Science Bulletin*, vol. 64, no. 1, pp. 8–10, Jan. 2019, doi: 10.1016/j.scib.2018.12.007.

[4] Ramadan, H. Bailliet, G. Poignand, and D. Gardner, "Design, manufacturing and testing of a compact thermoacoustic refrigerator," *Applied Thermal Engineering*, vol. 189, p. 116705, May 2021, doi: 10.1016/j.applthermaleng.2021.116705.

[5] X. Wang, J. Xu, Z. Wu, and E. Luo, "A thermoacoustic refrigerator with multiple-bypass expansion cooling configuration for natural gas liquefaction," *Applied Energy*, vol. 313, p. 118780, May 2022, doi: 10.1016/j.apenergy.2022.118780.

[6] J. J. Wollan, G. W. Swift, S. Backhaus, and D. L. Gardner, "DEVELOPMENT OF A THERMOACOUSTIC NATURAL GAS LIQUEFIER," p. 8.

[7] X. Xiao, X. Gu, and X. Zhang, "Combination of thermoacoustic heat dissipation with oscillating convection: A novel cooling method," *International Journal of Heat and Mass Transfer*, vol. 160, p. 120177, Oct. 2020, doi: 10.1016/j.ijheatmasstransfer.2020.120177.

[8] G. Chen and J. Xu, "Development of a small-scale piezoelectric-driven thermoacoustic cooler," *Applied Thermal Engineering*, vol. 213, p. 118667, Aug. 2022, doi: 10.1016/j.applthermaleng.2022.118667.

[9] O. G. Symko, E. Abdel-Rahman, Y. S. Kwon, M. Emmi, and R. Behunin, "Design and development of high-frequency thermoacoustic engines for thermal management in microelectronics," *Microelectronics Journal*, vol. 35, no. 2, pp. 185–191, Feb. 2004, doi: 10.1016/j.mejo.2003.09.017.

[10] R.-L. Chen, Y.-C. Chen, C.-L. Chen, C. Tsai, and J. DeNatale, "Development of miniature thermoacoustic refrigerators," in *40th AIAA Aerospace Sciences Meeting & Exhibit*, Reno,NV,U.S.A., Jan. 2002. doi: 10.2514/6.2002-206.

[11] N. Rott, "Damped and thermally driven acoustic oscillations in wide and narrow tubes," *Journal of Applied Mathematics and Physics (ZAMP)*, vol. 20, no. 2, pp. 230–243, Mar. 1969, doi: 10.1007/BF01595562.

[12] N. Rott, "Thermoacoustics," *Advances in applied mechanics*, vol. 20, 1980.

[13] G. W. Swift, "Thermoacoustic engines," p. 36.

[14] O. A. Al-Mufti and I. Janajreh, "Thermoacoustic Refrigeration: Short Review," *International Journal of Thermal and Environmental Engineering*, 2022.

[15] G. Chen, L. Tang, B. Mace, and Z. Yu, "Multi-physics coupling in thermoacoustic devices: A review," *Renewable and Sustainable Energy Reviews*, vol. 146, p. 111170, Aug. 2021, doi: 10.1016/j.rser.2021.111170.

[16] R. Rahpeima and R. Ebrahimi, "Numerical investigation of the effect of stack geometrical parameters and thermo-physical properties on performance of a standing wave thermoacoustic refrigerator," *Applied Thermal Engineering*, vol. 149, pp. 1203–1214, Feb. 2019, doi: 10.1016/j.applthermaleng.2018.12.093.

[17] D. Marx and P. Blanc-Benon, "Numerical Simulation of Stack-Heat Exchangers Coupling in a Thermoacoustic Refrigerator," *AIAA Journal*, vol. 42, no. 7, pp. 1338–1347, Jul. 2004, doi: 10.2514/1.4342.

[18] L. Zoontjens, C. Q. Howard, A. C. Zander, and B. S. Cazzolato, "Numerical comparison of thermoacoustic couples with modified stack plate edges," *International Journal of Heat and Mass Transfer*, vol. 51, no. 19–20, pp. 4829–4840, Sep. 2008, doi: 10.1016/j.ijheatmasstransfer.2008.02.037.

[19] N. Cao, J. R. Olson, G. W. Swift, and S. Chen, "Energy flux density in a thermoacoustic couple," *The Journal of the Acoustical Society of America*, vol. 99, no. 6, pp. 3456–3464, Jun. 1996, doi: 10.1121/1.414992.

[20] E. Besnoin, "Numerical Study of Thermoacoustic Heat Exchangers," 2001.

[21] T. Tisovsky and T. Vit, "Design of numerical model for thermoacoustic devices using OpenFOAM," Pilsen, Czech Republic, 2017, p. 020043. doi: 10.1063/1.5004377.

[22] H. Ishikawa and D. J. Mee, "Numerical investigations of flow and energy fields near a thermoacoustic couple," *The Journal of the Acoustical Society of America*, vol. 111, no. 2, pp. 831–839, Feb. 2002, doi: 10.1121/1.1430687.

[23] Abd El-Rahman and E. Abdel-Rahman, "Computational Fluid Dynamics Simulation of a Thermoacoustic Refrigerator," *Journal of Thermophysics and Heat Transfer*, vol. 28, no. 1, pp. 78–86, Jan. 2014, doi: 10.2514/1.T4150.

[24] Atchley, T. J. Hofler, M. L. Muzzerall, M. D. Kite, and C. Ao, "Acoustically generated temperature gradients in short plates," p. 13, Feb. 1990.

[25] S. Worlikar, O. M. Knio, and R. Klein, "Numerical Simulation of a Thermoacoustic Refrigerator II. Stratified Flow around the Stack," pp. 299–324, 1998.

[26] D. Marx and P. Blanc-Benon, "Computation of the temperature distortion in the stack of a standing-wave thermoacoustic refrigerator," *The Journal of the Acoustical Society of America*, vol. 118, no. 5, pp. 2993–2999, Nov. 2005, doi: 10.1121/1.2063087.